

THE  $7\frac{2}{3}$ -YEAR COLLECTION OF WELL-MONITORED FERMI-LAT GRB AFTERGLOWS

A. PANAITESCU

Space &amp; Remote Sensing, MS B244, Los Alamos National Laboratory, Los Alamos, NM 87545, USA

## ABSTRACT

We present the light-curves and spectra of 24 afterglows that have been monitored by Fermi-LAT at 0.1–100 GeV over more than a decade in time. All light-curves (except 130427) are consistent with a single power-law starting from their peaks, which occurred, in most cases, before the burst end. The light-curves display a brightness-decay rate correlation, with all but one (130427) of the bright afterglows decaying faster than the dimmer afterglows. We attribute this dichotomy to a quick deposition of the relativistic ejecta energy in the external-shock for the brighter/faster-decaying afterglows and to an extended energy-injection in the afterglow shock for the dimmer/slower-decaying light-curves. The spectra of six afterglows (090328, 100414, 110721, 110731, 130427, 140619B) indicate the existence of a harder component above a spectral dip/ankle at energy 0.3–3 GeV, offering evidence for an inverse-Compton emission at higher energies, and suggesting that the harder power-law spectra of five other LAT afterglows (130327B, 131231, 150523, 150627, 160509) could also be inverse-Compton, while the remaining softer LAT afterglows should be synchrotron. Marginal evidence for a spectral break and softening at higher energies is found for two afterglows (090902B and 090926).

*Subject headings:* radiation mechanisms: non-thermal, relativistic processes, shock waves – gamma-ray burst: general, individual

## 1. INTRODUCTION

Using the Fermi Science tools and the Fermi-LAT photon database, we identify 24 afterglows that have been followed by LAT over more than a decade in time. We construct the light-curves and spectra of those afterglows, visually search for correlations, fit them with simple power-laws (and broken power-laws for spectra), and compare the resulting fit indices/exponents with the expectations for the forward-shock model, all in an broad-brush attempt to identify generic features of that model that could explain the light-curve correlations and spectra features.

Our selection of well-monitored LAT afterglows, meaning afterglows monitored for more than a decade in time implies the exclusion of those afterglows that had a too fast fall-off after their first detection, especially if such afterglows were dim at early times (during the prompt-emission phase). From the First Fermi-LAT GRB catalog (Ackermann et al 2013a), 10 afterglows that display a long-monitored light-curve are included in the current sample. To those, we add another 14 afterglows with well-monitored light-curves, the current sample containing 21 percent of the 108 afterglows detected by LAT during the first  $7\frac{2}{3}$  years. In other words, LAT detects on average one GRB afterglow per month, but only one out of four (about 3/year on average) is a well-monitored afterglow.

In addition to the First LAT GRB catalog, the LAT light-curves and spectra of some of the afterglows in our sample have been previously published in other articles: 080916C (Abdo et al 2009a), 090217 (Ackermann et al 2010b), 090510 (Ackermann et al 2010a, Ghirlanda, Ghisellini, Nava 2010), 090902B (Abdo et al 2009b), 090926 (Swenson et al 2010, Ackermann et al 2011), 110721 (Axelsson et al 2012), 110731 (Ackermann et al 2013b), 130427 (Fan et al 2013, Tam et al 2013, Ackermann et al 2014), 130821 (Liang et al 2014), 131231 (Liu et al 2014). The afterglows 090510 and 131108 have also been observed above 100 MeV by AGILE (Giuliani et al 2010, Giuliani et al 2014).

## 2. HOW AFTERGLOW LIGHT-CURVES AND SPECTRA ARE CALCULATED AND FIT

The "event" and "spacecraft" data used here were downloaded from the Fermi-LAT database at <http://fermi.gsfc.nasa.gov/cgi-bin/ssc/LAT/LATDataQuery.cgi> and processed using the Fermi Science tools at [fermi.gsfc.nasa.gov/ssc/data/analysis/scitools/references.html](http://fermi.gsfc.nasa.gov/ssc/data/analysis/scitools/references.html). The event files are downloaded with "extended" option that includes "transient"-class photons, having more background. The transient-class photons are used in the construction of afterglow light-curves, while spectra are obtained using "source"-class photons that have a lower background.

Selection cuts on the event data files are done using the GTSELECT tool. The cuts include: selection of photon-class (16 for transient, 128 for source) above 100 MeV, within a Search Region radius of  $10^\circ$  around the burst location, starting at the burst trigger time, and exclusion of photons close to Earth's limb (at zenith angle  $112^\circ$ ). Events within the time range when the data are valid are retained using the GTMKTIME tool. Tool GTBINDEF is used to create the logarithmic time and energy-grids for light-curves and spectra. Photon counts with specified time-binning are obtained using the GTBIN[LC] tool and the full-exposure (LAT effective-area, i.e. integrated over the afterglow spectrum and corresponding to the photon incidence angle at each time, multiplied by the exposure-time corresponding to each time-bin) are added to the light-curve file using the GTEXPOSURE tool and the appropriate instrument response function: P8R2\_TRANSIENT020\_V6 for transient-class photons and P8R2\_SOURCE\_V6 for source-class photons. Photon fluxes above 100 MeV are calculated by dividing photon counts by the full-exposure of each time-bin. Photon counts on a given time and energy-grid are calculated with GTBIN[PHA2] tool, from where spectra are obtained by dividing by the full-exposure calculated with the GTEXPOSURE tool on the spectral time-binning. Spectra are corrected for the LAT effective-area dependence on the photon energy (fig 15 of Atwood et al 2009), which for photons at normal incidence can be well-

approximated by  $A(E < 1\text{GeV}) = A_0[1 + 0.6 \log(E/\text{GeV})]$  and  $A(E > 1\text{GeV}) \simeq A_0$ , the coefficient 0.6 having a weak dependence on the incidence angle  $\theta$  (e.g. it is 0.7 for  $\theta = 60^\circ$ ).

Figure 1 shows the light-curves and spectra of GRB afterglow 130427, and assesses the effects of using transient or source-class photons, as well as that of the size of the region around the source over which photons are counted. Detector background photons account for 46 percent of the transient-class photons in the lowest energy channel (100 MeV) shown in the right-upper panel, with that proportion decreasing strongly with photon energy, such that there are no background photons above 2 GeV (i.e. all transient-class photons are source-class). Consequently, spectra built with source-class photons are slightly harder than those constructed with transient-class photons. The effect on light-curves (left-upper panel) is often un-noticeable because, in the calculation of the full-exposure, we used the detector response-function corresponding to each photon class.

Afterglow light-curves are calculated within a search area radius of  $10^\circ$  around the burst, but a search area of only  $5^\circ$  is used for dimmer afterglows that reach the background in less than a decade in time after the peak or after the first measurement. If that background is mostly the isotropic celestial background, then a reduction by a factor two in the search radius lowers the background by a factor four, which, for a flux decay  $F \propto t^{-1}$ , extends by 0.5 dex the measurement of the afterglow power-law flux decay before it becomes lost in the background. An ever stronger reduction of the background results if most of that background is from a steady source near the burst. That is the case for GRBs 110731, 130327B, 150902, and 150627, which are at several degrees from the Galactic plane, and for GRBs 150523 and 150627 which occurred at  $7^\circ$  off the Vela pulsar.

The LAT point-spread function being  $PSF(E) = 3.5^\circ(E/100\text{MeV})^{-0.8}$  for on-axis photons, and having a slow increase with the incidence angle (e.g. the coefficient is  $5^\circ$  for  $\theta = 60^\circ$  – fig 17 of Atwood et al 2009), means that a source-region of  $5^\circ$  misses about 1/3 of the 100 MeV photons, while a  $10^\circ$  region loses about 5 percent of same photons, with the loss of photons being negligible above 200 MeV, for which  $PSF(E > 200\text{MeV}) < 2 - 3^\circ$ . Therefore, using a source region of only  $5^\circ$  (for the reasons discussed above) leads to a small flux decrease (see light-curves in the lower-right panel of Fig 1), and the corresponding loss of predominantly lower energy photons yields slightly harder spectra (as illustrated in the right-lower panel).

In summary of the above and of Figure 1, light-curves will be calculated using transient-class photons integrated over  $5^\circ$  or  $10^\circ$  around the source although neither the choice of photon class nor the size of the source region affect much the index of the afterglow flux power-law decay, while spectra are calculated using source-class photons integrated over  $10^\circ$  around the source, in order to obtain a reliable spectral slope, although that aim will be too often defeated by the paucity of high-energy photons (above 1 GeV), which will lead to uncertainties in the best-fit power-law exponent that exceed the accuracy  $\Delta\beta \lesssim 0.2$  allowed by the use of (lower background) source-class photons.

The afterglow light-curves and spectra obtained with the Fermi Science tools as described above are fit with power-laws, as is routinely done for GRB afterglows observed at lower photon energies: radio (1–100 GHz), optical (1–3 eV), or X-ray (1–10 keV). Power-law spectra are expected for the

emission from shock-accelerated electrons, whose distribution with energy is a power-law  $dN_e/dE \propto E^{-p}$ . Then, synchrotron energy-spectra from such electrons will be a power-law  $E(dN_\gamma/dE) \propto E^{-\beta}$  with the spectral index  $\beta = (p-1)/2$ . Adding to such power-law spectra a power-law dynamics of the source (i.e. Lorentz factor and number of emitting electrons that evolve as power-laws in observer-time) leads to power-law afterglow light-curves  $dN_\gamma/dt \propto t^{-\alpha}$ , as predicted by Mészáros & Rees (1997) for the synchrotron emission from an adiabatic forward-shock driven by a relativistic outflow in the circumburst medium (see also Kumar & Barniol Duran 2009) and for the synchrotron emission from cooling electrons that were accelerated by the reverse-shock crossing the GRB outflow at early times. The power-law light-curves also stand for non-adiabatic shocks provided that energy is added (Rees & Mészáros 1998) to the external shock (reverse and forward shocks) in a power-law fashion. The upscattering of a power-law synchrotron spectrum by a power-law distribution of electrons leads to power-law inverse-Compton spectra (one of the input power-law suffices) of same slopes as the synchrotron spectrum and to power-law light-curves of steeper decay (larger index  $\alpha$ ), as shown in table 2 of Panaitescu & Vestrand (2012).

The following are worth mentioning about the sample selection and power-law fits to their light-curves and spectra.

Our selection of long-monitored LAT afterglows excludes afterglows whose flux exhibits a too fast decay into the background, similar to a typical X-ray light-curve measured by Swift-XRT. With three exceptions (GRBs 090510, 110731, 130427), all other light-curves are well fit by a single power-law ( $\chi^2_\nu \lesssim 1$ ) from their peaks to the last measurement above the background, 130427 being the only afterglow with a light-curve break, the other two exceptions displaying a single fluctuation above a power-law decaying flux, after the burst for 090510, at the burst end for 110734.

Spectra are fit with a power-law starting from the lowest energy channel (100 MeV) and up to highest energy for which the measurement is not more than  $1\sigma$  above the power-law fit. Spectra are not always fit up to the highest energy channel (100 GeV), with the higher energy channels having sometimes only a flux  $1\sigma$  upper limit, even if the resulting fit were acceptable. That is done for a few reasons, all related to the possible existence of a hard spectral component at higher energies (above few GeV). One reason is that the power-law fit illustrates better the existence of that hard component. Second reason is that  $\chi^2$  overestimates the fit quality when some channel fluxes lie predominantly on one side of the power-law fit. Third reason is to determine accurately the spectral slope  $\beta$  at the lower energy channels, where most photons are, because that is the slope that should be related to the index  $\alpha$  of the afterglow flux power-law decay.

Power-law best-fits are determined by minimizing

$$\chi^2 = \sum_i \left( \frac{F_{obs,i} - F_{pl,i}}{\sigma_i} \right)^2 \quad (1)$$

where  $F_{obs,i}$  is the measured flux,  $F_{pl,i}$  is the power-law model flux. For light-curves,  $\sigma_i$  is the  $1\sigma$  uncertainty of the photon flux  $F_{obs,i} \equiv dN/dt$ , but for spectra it is the Poisson statistics uncertainty of the model power-per-decade  $F_{pl,i} \equiv$

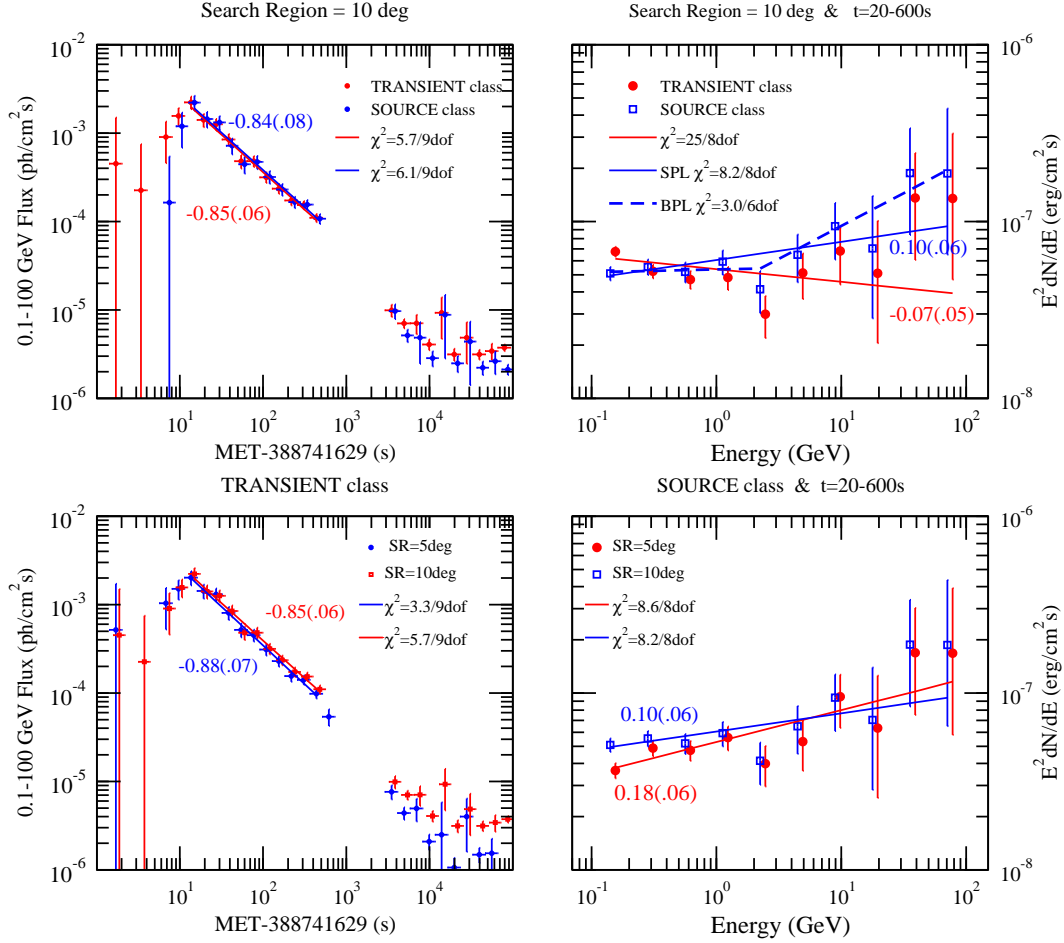


FIG. 1.— Comparison of light-curves (left column) and spectra (right column) for the GRB afterglow 130427A obtained with TRANSIENT-class and SOURCE-class photons (upper row) and for a SOURCE REGION of  $5^\circ$  and  $10^\circ$  (lower row). *Right row*: spectra  $E^2(dN/dE) \propto E^{1-\beta}$  are fit with single power-laws, with the best-fit exponent  $1 - \beta$  indicated. *Left row*: light-curves for photons above 100 MeV are fit with a single power-law  $t^{-\alpha}$  over the time-range 20–600s, the best-fit decay exponent  $-\alpha$  and its uncertainty being indicated. (At 600–3000s, the afterglow is behind by the Earth.) After 10 ks, most LAT photons are the celestial background, consistent with the factor four difference between the photon fluxes in source regions of  $5^\circ$  and  $10^\circ$  shown in the lower-left panel. *Upper panels*: transient-class photons contain more detector background than source-class photons, but that does not change significantly the light-curve decay index  $\alpha$  (upper-left panel). Because most instrument background photons are at low energy, their removal leads to source-class spectra that are harder than transient-class spectra by  $\Delta\beta = -0.17 \pm 0.08$  (right-upper panel). *Lower panels*: because  $PSF(100\text{ MeV}) = 5^\circ$ , increasing the source-region size from  $5^\circ$  to  $10^\circ$  increases slightly the photon flux but leaves unchanged the flux decay index  $\alpha$  (lower-left panel); adding that LAT’s  $PSF(E) \propto E^{-0.8}$ , means that doubling the source-region size leads to a softer spectrum, by  $\Delta\beta = 0.16 \pm 0.11$  (lower-right panel). *Upper-right panel*: the reduction of  $\Delta\chi^2 = 2.8$  in the chi-square from a *single* power-law fit (blue solid line) to the 20–600 s source-class photon spectrum to a *broken* power-law fit (dashed black line) has a 1.8 percent probability of occurring by chance (according to the  $F$ -test). The broken power-law best-fit has a break energy  $E_* \simeq 2$  GeV and spectral slopes below and above the ankle are  $\beta_{lo} = 1.0$  and  $\beta_{hi} = 0.6$ . Ackermann et al (2014) have identified a hard spectral component with  $\beta = -1/3$  at earlier times, 4.5–11.5 s, during the prompt emission phase.

$E^2(dN/dE)_{pl}$ :

$$\sigma\left(E^2 \frac{dN}{dE}\right) = E^2 \frac{\sigma(C_{pl})}{\Delta E A \Delta t} = E \sqrt{\frac{E^2(dN/dE)_{pl}}{\Delta E A \Delta t}} \quad (2)$$

where  $\sigma(C_{pl}) = \sqrt{C_{pl}}$  and  $C_{pl} = (dN/dE) \Delta E A \Delta t$  is the model photon-count in channel of energy  $E$ ,  $\Delta E$  being the width of that channel,  $\Delta t$  the spectrum integration-time, and  $A$  the detector effective area ( $A \Delta t$  is the full-exposure calculated by the GTEXPOSURE tool).

The reason for using the model flux uncertainty instead of the measurement uncertainty obtained with the GTBIN tool is that the latter is calculated by summing over Poisson distributions of all integer average flux  $C_o$ , each distribution being weighted by the Poisson probability of measuring a flux

$C_{obs}$  if the true flux were  $C_o$ .<sup>1</sup> Consequently, for lower-energy channels (below 1 GeV), which often have few/several photons, the weighted-Poisson uncertainty calculated by GTBIN is  $\sigma_{gtbin}(C_{obs}) \simeq \sqrt{C_{obs}}$  and Poisson statistics for the power-law model counts  $C_{pl}$  (which is equal with the measured counts  $C_{obs}$  when the best-fit is reached) is good enough for estimating the measurement uncertainty and for using in the  $\chi^2$  calculation. However, for higher-energy channels (above 1 GeV), which always have a few photons,  $\sigma_{gtbin}(C_{obs}) > \sqrt{C_{obs}}$  and the use of measurement errors calculated by GTBIN would give little weight to the high-energy channels in determining the best-fit power-law. In that case, the use of model count uncertainty leads to a more accurate determination of the best-fit power-law index.

<sup>1</sup>One reason for why GTBIN calculates the measurement uncertainty in this way could be that, for a non-detection  $C_{obs} = 0$ , the Poisson distribution of average  $C_0 = 0$  is a  $\delta$  function, whose dispersion  $\sigma = 0$  is un-usable. Another reason is that  $C_{obs}$  photons being detected does not imply that the measurement was drawn only from a Poisson distribution of average/peak value  $C_{obs}$ .

$1\sigma$  uncertainties of the exponent of the best-fit power-law to light-curves and spectra are determined from an increase  $\Delta\chi^2 = 2.3$  above the minimal  $\chi^2$  of the best-fit, i.e. the uncertainties are calculated for the joint variation of both fit parameters (normalization and power-law index). These uncertainties are about 50 percent larger than those obtained by varying only one parameter of interest (the slope), which corresponds to  $\Delta\chi^2 = 1$ .

### 3. AFTERGLOW LIGHT-CURVES

The power-law fits to the light-curves and spectra of 24 well-monitored LAT afterglows are shown in Figures 2 and 3, and the best-fit power-law exponents are listed in Table 1. About two-thirds of light-curves show that the LAT light-curve peak occurred during the burst and the light-curves do not show any deviation from a power-law at the end of the burst, indicating that the prompt emission mechanism does not contribute much to LAT emission above 100 MeV after the light-curve peak. This implies that, for a majority of afterglows in our sample, the LAT *post-peak* emission is a spectral component brighter than the extrapolation to 100 MeV of the Band spectrum of the prompt/burst MeV emission. The joint spectral analysis of Fermi-GBM and LAT data during the burst phase shows that to be the case for GRB 080916C (Abdo et al 2009a), GRB 090510 (Ackermann et al 2010a, Giuliani et al 2010), GRB 090902B (Abdo et al 2009b), GRB 090926 (Ackermann et al 2011), GRB 110731 (Ackermann et al 2013b), GRB 130427 (Ackermann et al 2014), GRB 131108 (Giuliani et al 2014), but there is also a claim that the Band function describes well the entire GBM and LAT burst measurements over five decades in energy, for GRB 090217 (Ackermann et al 2010b).

All fits are plotted together in Figure 4 (left panel), which suggests a correlation between the afterglow brightness and its decay: brighter afterglows decay faster than dimmer afterglows. For the fast-decaying afterglows with  $\alpha > 1$ , most of their energy release occurs at the light-curve peak, while for slow-decaying afterglows with  $\alpha < 1$ , most of their energy release occurs well after the peak. Part of the above correlation is a selection effect because retaining only afterglows that have been long monitored excludes dimmer afterglows with a fast fall-off, as they get below the background in less than a decade in time since first detection. However, the rest of that correlation is real: bright afterglows with a slow dimming rate are absent, with the exception of 130427. Given that the brightness distribution at 10 s has a width of 2 dex, which is at least 1 dex more than what the spread by a factor 2-3 in redshift can induce, the brightness-decay correlation implies a luminosity-decay correlation.

A similar correlation was observed for the optical emission of afterglows displaying an early fast-rise to a peak at about 100s (Panaitescu & Vestrand 2008). The energetic output of the brighter/fast-falling optical light-curves was found to be better correlated with the GRB output than for the dimmer/slowly-decaying optical light-curves (Panaitescu & Vestrand 2011), which suggests that the above dichotomy (bright+fast decays and dim+ slow-decays) of optical afterglows is due to how the outflow energy is deposited in the external shock: impulsive outflows (released on a short timescale) lead to bright optical afterglows (because all outflow's energy was quickly deposited in the shock) while extended outflows yield dimmer optical afterglows (because only a fraction of the entire outflow energy was in the afterglow shock at early times) and to a slower-decaying

optical light-curves (because of the long-lived energy injection in the external shock).

We extend the above conclusion reached with a sample of 33 optical afterglows to the current 24 LAT afterglows, and attribute the bright/faster-decaying afterglows to an impulsive release of the relativistic ejecta and the dimmer/slower-decaying afterglows to an extended ejecta release.

For more than half of the light-curves of Figures 2 and 3, the 1–50 s LAT light-curve peak occurs during the prompt GRB emission. Optical light-curves also display peaks, but at later times (50–1000s). The difference in peaks epochs is due to 1) a selection bias against late LAT peaks, which may be too dim to allow a long-monitoring of the afterglow, and 2) an observational bias against early optical peaks, which may be missed due to the latency of robotic optical telescopes to respond to GRB trigger notices. A minority of Swift X-ray afterglow light-curves also display a peak after 100 s (Panaitescu, Vestrand, Wozniak 2013), because peaks occurring earlier are overshadowed by the prompt emission.

Therefore, LAT afterglow observations are best to catch the earlier light-curve peaks. As for the optical and X-ray light-curve peaks, we propose that the most likely reason for the LAT peaks is the onset of the forward-shock deceleration, although other explanations are possible: 1) light-curve peaks at any observing frequency arise if the direction toward the observer is not initially within the jet opening, when the jet has decelerated enough that the direction toward the observer has entered the relativistically-beamed emission cone, 2) LAT light-curve peaks could be due to the emission above 100 MeV becoming optically-thin to pair-formation.

If light-curve peaks arise from the onset of deceleration, then the peak epoch is

$$t_p = (z+1) \frac{R_d}{2c\Gamma_0^2} = 16 \frac{z+1}{3} \left( \frac{E_k(t_p)}{10^{53} \text{ erg}} \frac{1 \text{ cm}^{-3}}{n} \right)^{1/3} \left( \frac{\Gamma_0}{400} \right)^{-8/3} s \quad (3)$$

where  $E_k$  is the isotropic-equivalent kinetic energy of forward-shock at time  $t_p$ ,  $\Gamma_0$  is the ejecta initial Lorentz factor,  $z$  is the afterglow redshift, and  $n$  is the external medium proton density at the deceleration radius  $R_d$ , where the forward-shock has swept-up a mass  $\Gamma_0$  smaller than that of the ejecta. Panaitescu et al (2013) have shown that variations in the ambient medium density among afterglows lead to a peak-flux  $F_p$  – peak-epoch  $t_p$  anticorrelation consistent with that measured for 30 optical peaks:  $F_p \propto t_p^{-(2-3)}$ . Variations in  $\Gamma_0$  lead to an anticorrelation of a smaller slope, while those in  $E_k$  produce a correlation. Performing the same test with LAT light-curves requires more than the seven light-curve peaks (shown in Figures 2 and 3) of afterglows with known redshift.

Continuing with the generally-accepted identification of the LAT afterglow emission with the forward-shock's (e.g. Kumar & Zhang 2015), we compare in Figure 4 (right panel) the temporal and spectral power-law indices ( $\alpha, \beta$ ) with the expectations for that model. The forward-shock model predicts a closure-relation  $\alpha = k\beta + c$  with  $k$  depending on the shock geometry (spherical, conical jet, sideways spreading jet) and radiation mechanism (synchrotron, inverse-Compton) dominant at the observing frequency and  $c$  depending on the radiation mechanism, radial distribution/stratification of the ambient medium (homogeneous, wind-like), and location of the observing frequency relative to the breaks (peak, cooling) of the afterglow

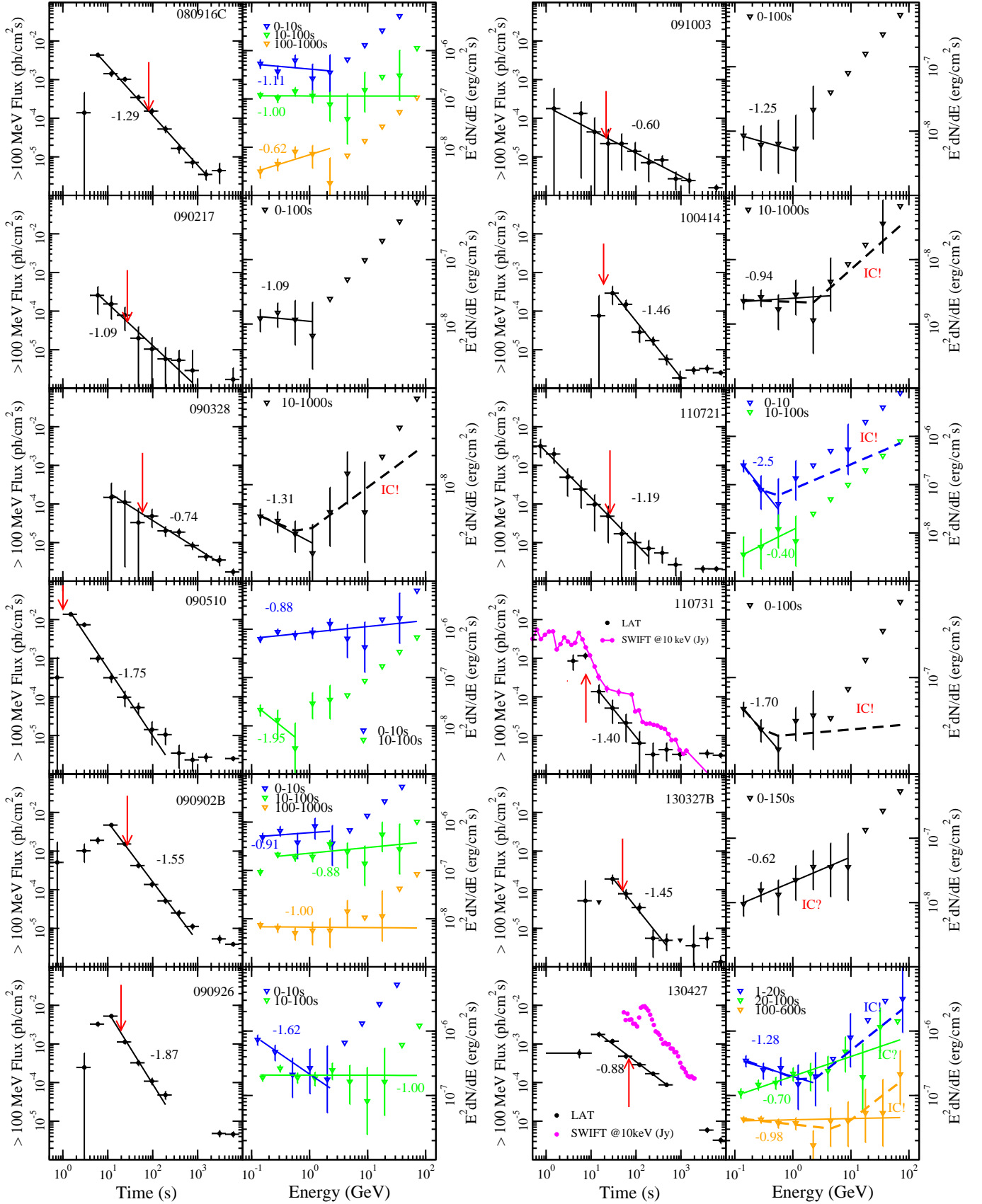


FIG. 2.— Light-curves above 100 MeV (left panels) and 0.1–100 GeV power-per-decade spectra (right panels) for 12 afterglows whose power-law flux decays have been monitored by Fermi-LAT over at least one decade in time. *Light-curves* time-bins extend over a factor two (0.3 dex). The red arrow indicates the end of the prompt-emission phase (the burst). The 10 keV flux (in Jy) for Swift afterglows is also shown. Numbers give the exponent  $-\alpha$  of the power-law flux decay (Table 1). Triangles denote  $1\sigma$  upper limits, and correspond to 1.9 photons. (continued in next figure)

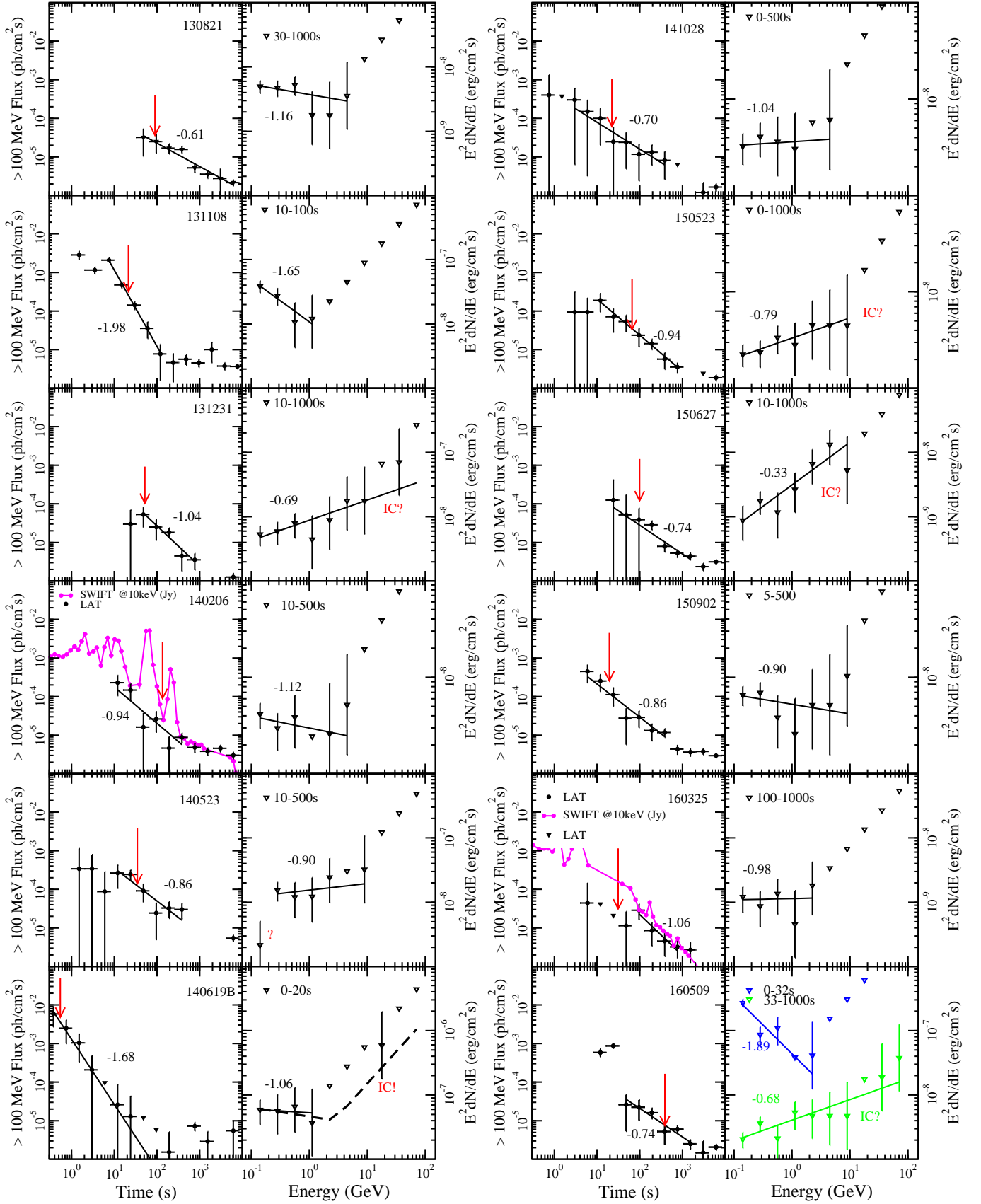


FIG. 3.— Same as in Figure 2, for another 12 afterglows well-monitored by LAT. *Spectral energy-bins* extend over a factor two. Single power-law fits are made starting from 100 MeV and up to where measurements can be fit within their error. Numbers give the slope  $-\beta$  of the power-law  $F_E$  spectrum (Table 1). Triangles without error bars show  $1\sigma$  upper limits. (Because the GTBIN tool assigns a statistical uncertainty of 1.9 photons for any non-detection and because the energy channel binning used here satisfies  $\Delta E \propto E$ , all non-detections follow  $E^2(dN/dE) \propto E$ ). Dashed lines show broken power-law fits (labeled “IC!”) for which the higher-energy harder component was found to have a confidence level of at least 90 percent (Table 2). Spectra harder than  $F_E \propto E^{-1}$  (labeled “IC?”) are also candidates for inverse-Compton emission. For 130427, we find good evidence for inverse-Compton above the spectral break at 1–20s and at 100–600s, and also in

TABLE 1

Indices of power-law fits to the light-curves  $dN/dt \propto t^{-\alpha}$  and spectra  $F_E = E(dN/dE) \propto E^{-\beta}$  of GRB afterglows that have been followed-up by Fermi-LAT over at least a decade in time.  $1\sigma$  uncertainties of the best-fit slopes are for the joint variation of both fit-parameters (slope and normalization).  $\Delta t$  is the time interval over which the power-law fit was done. The power-law spectrum fit is over the lower energy channels where all measurements are within their  $1\sigma$  uncertainty of the model flux (see Figures 2 and 3).

LIGHT-CURVE					SPECTRUM				
GRB	$\Delta t(s)$	$\alpha(\sigma_\alpha)$	$\Delta t(s)$	$\beta(\sigma_\beta)$	GRB	$\Delta t(s)$	$\alpha(\sigma_\alpha)$	$\Delta t(s)$	$\beta(\sigma_\beta)$
080916C	4-2000	1.29(.05)	1-1000	1.01(.09)	090217	4-1000	1.09(.42)	1-100	1.09(.47)
090328	10-4000	0.74(.13)	10-1000	1.31(.28)	090510	1-130	1.77(.11)	1-100	0.91(.09)
090902B	10-700	1.60(.08)	1-700	0.95(.08)	090926	10-250	1.87(.13)	1-100	1.11(.09)
091003	1-2000	0.60(.21)	1-100	1.25(.53)	100414	25-1000	1.46(.21)	10-1000	1.06(.21)
110721	0.5-200	1.19(.22)	1-100	1.35(.33)	110731	10-150	1.43(.65)	1-100	1.70(.35)
130327B	20-500	1.45(.26)	10-160	0.62(.13)	130427	10-600	0.88(.06)	20-600	1.17(.06)
130821	30-7000	0.61(.12)	1-600	1.16(.23)	131108	5-150	1.98(.22)	10-100	1.65(.35)
131231	30-1000	1.04(.34)	10-300	0.69(.16)	140206	10-400	0.94(.38)	10-400	1.12(.26)
140523	10-500	0.85(.36)	10-500	0.90(.28)	140619B	0.3-30	1.66(.46)	1-20	1.06(.50)
141028	2-400	0.70(.50)	1-400	0.94(.29)	150523	10-1000	0.94(.18)	1-1000	0.79(.17)
150627	20-2000	0.74(.32)	1-1000	0.34(.17)	150902	5-400	0.86(.24)	1-500	1.10(.19)
160325	90-1000	1.06(.70)	90-1000	0.98(.30)	160509	30-1000	0.74(.20)	30-1000	0.68(.12)

TABLE 2

Results of the  $F$ -test for the statistical significance of the high-energy harder spectral component.  $\Delta t$  is the spectrum integration time,  $\chi^2_{spl}$  and  $\chi^2_{bpl}$  are for the single power-law and broken power-law best-fits to ten-energies channels.  $E_*$  is the best-fit value for the dip energy, above which the spectrum hardens, and its  $1\sigma$  range was determined by a  $\Delta\chi^2 = 1$  increase around the best fit.

GRB	$\Delta t$ (s)	$\chi^2_{spl}$ (8 df)	$\chi^2_{bpl}$ (6 df)	BPL prob	$E_*$ (GeV)	$\sigma(E_*)$ (GeV)	GRB	$\Delta t$ (s)	$\chi^2_{spl}$ (8 df)	$\chi^2_{bpl}$ (6 df)	BPL prob	$E_*$ (GeV)	$\sigma(E_*)$ (GeV)
090328	10-1000	10.4	6.5	0.90	0.8	0.4-1.4	100414	10-1000	12.1	6.0	0.95	2.3	1.2-14
110721	0-10	13.6	3.6	0.994	0.4	0.2-0.6	110731	0-100	7.8	4.9	0.90	0.4	0.2-0.7
130427	1-20	14.8	4.3	0.992	1.9	0.9-5.1	140619B	0-20	6.1	3.4	0.93	2.7	0.8-8.5

spectrum (see table 2 of Panaitescu & Vestrand 2012 for all possible values of  $c$  and  $k$ , including also the effect of energy injection in the blast-wave). Thus, the  $\alpha - \beta$  correlation expected for the forward-shock is that softer afterglows should decay faster.

The linear correlation coefficient of the decay indices and spectral slopes shown in Figure 4 is  $r = 0.29 \pm 0.26$ . A similarly weak correlation is manifested by Swift X-ray afterglows at early times (figure 4 of Panaitescu 2007). The  $r = 0.29$  corresponds to a 20 percent probability of this correlation occurring by chance, and the weakness of this correlation could be due to 1) more than one forward-shock sub-model occurring in LAT afterglows and to 2) the limited baseline of both indices. The large  $\sigma_r \lesssim r$  reflects the substantial uncertainties of one or both indices and makes the  $\alpha - \beta$  correlation only marginally significant.

Given the large uncertainty in the temporal and spectral indices shown in Figure 4, nearly all LAT afterglows are consistent with a forward-shock without energy injection. Still, half of the slowly-decaying LAT afterglows ( $\alpha < 1$ ) display decays slower than for the slowest decay expected from an adiabatic forward-shock (synchrotron emission with synchrotron cooling energy below 100 MeV). Thus, Figure 4 offers some evidence for a sustained energy-injection in the forward-shock.

Last note about the light-curves shown in Figures 2 and 3 is that the LAT flux decay appears to be consistent with the con-

temporaneous light-curve measured by Swift-XRT at 1–10 keV in four cases, to the extent that the X-ray flares present in all those four afterglows can be ignored. We note that six LAT afterglows display a flux-decay slower than  $dN/dt \propto t^{-3/4}$ , which would be the LAT counterpart of the X-ray plateaus seen by Swift-XRT in a many afterglows (e.g. Nousek et al 2006).

#### 4. AFTERGLOW SPECTRA

##### 4.1. High-energy hard spectral component from inverse-Compton

Out of the 24 LAT afterglows considered here, we find evidence (above 90 percent confidence level) of a harder component at higher-energies (above a dip or ankle energy) in six cases, which are listed in Table 2. With  $\Delta\chi^2 = \chi^2_{spl} - \chi^2_{bpl}$  the reduction in  $\chi^2$  produced by the addition of another power-law at higher energies and the reduced chi-square  $\chi^2_\nu = \chi^2_{bpl}/\nu$  of the broken power-law fit, the probability that the  $\Delta\chi^2$  reduction is accidental follows the  $F$ -distribution  $P(F; 1, \nu)$ , where  $F = \Delta\chi^2/\chi^2_\nu$  and  $\nu = 6$  is the number of degrees of freedom for the broken power-law fit (10-channel fluxes minus four model parameters). Then,  $1 - P(F; 1, 6)$  is the probability for the hard spectral component being real (listed in Table 2).

If both spectral components are from the same shock, then it seems natural to conclude that the lower-energy component is synchrotron and the higher-energy component is inverse-



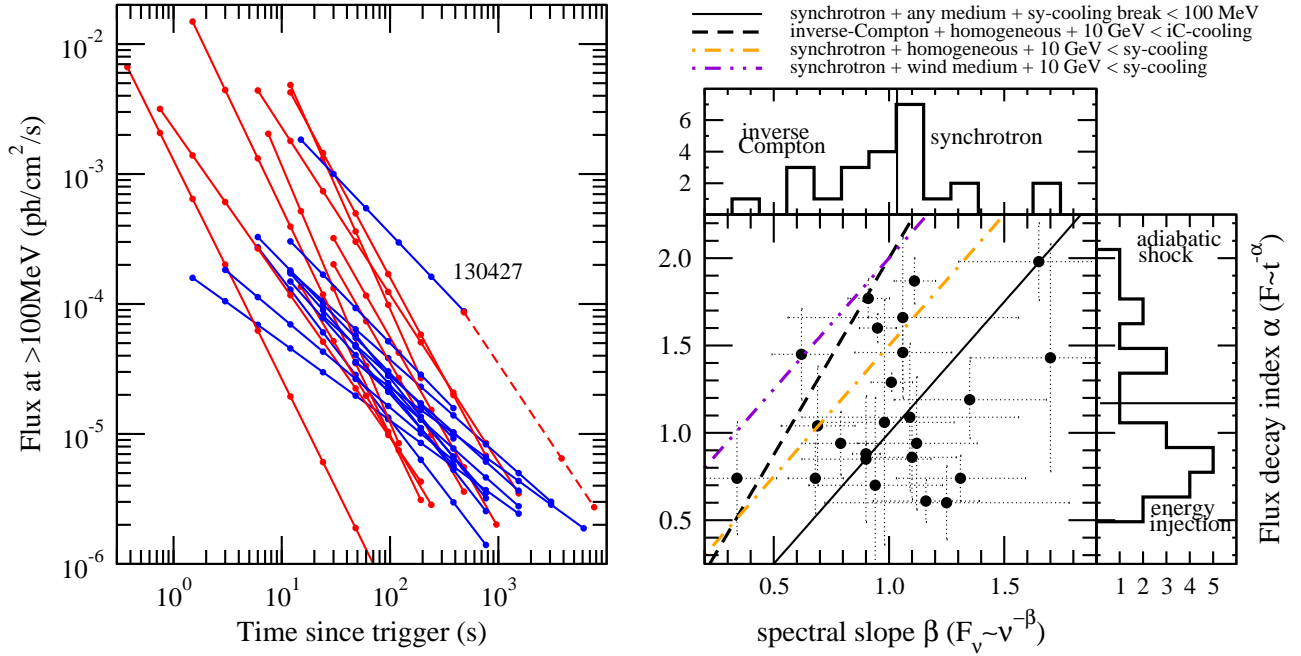


FIG. 4.— *Left panel*: 24 LAT afterglow light-curves, with fast decayers ( $\alpha < -1.2$ ) shown in red and slow decayers ( $\alpha > -1.2$ ) in blue. 130427 is the only case with a clear light-curve break/steepening, and its break at 4 ks is chromatic, not seen at any other wavelength (optical or X-ray). *Right panel*: flux decay-index  $\alpha$  vs the index  $\beta$  of the power-law energy spectrum. Dots show  $1\sigma$  uncertainties. Lines indicate the  $\alpha - \beta$  relation expected for the synchrotron and inverse-Compton emissions from an adiabatic forward-shock interacting with a homogeneous medium or a wind-like one, with the LAT range being located below or above the spectral cooling-break corresponding to the electrons whose radiative cooling-time equals the timescale over which a new generation is produced (i.e. the afterglow dynamical timescale). Lines in the histograms of indices  $\alpha$  and  $\beta$  show the corresponding average values. Faster-decaying light-curves may be associated with an impulsive ejecta release, while slower-decaying afterglows with energy injection in the forward-shock. Harder spectra could be inverse-Compton dominating the LAT emission, while softer spectra are more likely to be synchrotron emission.

Compton. At such high energies, the afterglow synchrotron emission is most likely measured above the cooling break, where the spectral slope of  $F_E$  is  $\beta_l = p/2$ , with  $p$  being the index of the power-law distribution of electrons with energy in the shock. For the higher-energy component to be harder than the synchrotron emission at lower energies, the inverse-Compton spectrum must be measured by LAT below the upscattered cooling break, where the spectral slope is  $\beta_h = (p - 1)/2$ . Therefore, in this interpretation of the spectral dip of the six afterglows of Table 2, one expects a spectral hardening across that dip by  $\beta_h - \beta_l = 1/2$ , which is compatible with (or less than) the hardening  $\Delta\beta$  displayed by the spectra of Figures 2 and 3, but not clearly inconsistent with them because the high-energy spectral slope is very uncertain.

If this synchrotron self-Compton interpretation of the LAT spectra with a break is correct, and if the LAT emission arises in the forward-shock, then the dip energy  $E_*$  can be calculated by equating the synchrotron and inverse-Compton fluxes:  $F_{sy}(E_*) = F_{iC}(E_*)$ , leading to  $E_* = E_c^{(sy)}/Y^2$  for  $\beta = 1$ , with  $E_c^{(sy)}$  the cooling-break energy of the synchrotron spectrum and  $Y < 1$  the Compton parameter. From here, one obtains

$$E_* = 1 \left( \frac{E_k}{10^{53} \text{ erg}} \right)^{-1} \left( \frac{\varepsilon_e}{10^{-3}} \right)^{-2} \left( \frac{\varepsilon_B}{10^{-5} \text{ 1 cm}^{-3}} \frac{n}{1} \right)^{-1.5} \text{ GeV} \quad (4)$$

for a homogeneous external medium of proton density  $n$  (in this

case,  $E_*$  is time-independent) and

$$E_* = 5 \left( \frac{E_k}{10^{53} \text{ erg}} \right)^{0.5} \left( \frac{\varepsilon_e}{10^{-3}} \right)^{-2} \left( \frac{10^{-9} \text{ t}}{\varepsilon_B \text{ 100 s}} \right)^{1.5} \text{ GeV} \quad (5)$$

for the  $n \propto r^{-2}$  wind of a Wolf-Rayet star (as the GRB progenitor), with  $E_k$  the forward-shock kinetic energy,  $\varepsilon_e$  and  $\varepsilon_B$  the post-shock fractional energies in electrons and magnetic field, respectively, and redshift  $z = 1$  was assumed.<sup>2</sup> The above equations indicate that, if the shock is adiabatic (no energy-injection) and if the two micro-parameters do not evolve, then the dip energy  $E_*$  is constant for a homogeneous medium and increases for a wind-like medium. The multi-epoch spectra of Figures 2 and 3 provide a very weak support for a constant or a decreasing dip energy  $E_*$ .

Also from the above two equations, it is evident that  $E_*$  may fall below 100 MeV, in which case all LAT emission would be inverse-Compton. Because the synchrotron spectrum above 100 MeV can only be softer than the inverse-Compton, it seems natural to correlate the hardness of LAT spectra with the afterglow emission process and attribute spectra softer (harder) than  $\beta = 1$  to synchrotron (inverse-Compton). Afterglows 130327B, 131231, 150523, 150627, and 160509, as well as 130427 at the second epoch shown in Figure 2, display a hard power-law over the entire LAT range; we suggest that the LAT emission of those afterglows was inverse-Compton.

<sup>2</sup>The wind case requires a very weak magnetic field in the forward-shock, especially if  $\varepsilon_e \gtrsim 0.01$ , as obtained from modeling the afterglow broadband emission.



#### 4.2. Spectral steepening due to photon-photon absorption

If the high-energy afterglow emission is optically-thick to pair-formation above an energy  $E_\tau$  that falls within the LAT range, then a steepening of the spectrum above that "cut-off" energy should be observed. This attenuation is most likely to be seen early during the afterglow, when the source is smaller and the pair-formation opacity larger. Assuming that the source Lorentz factor is of at least a few hundreds, an observed 1 GeV photon will form pairs with photons of threshold-energy above 10 MeV. While there could be a measurable output above 10 MeV from the sub-MeV burst mechanism, those target photons are dimmer than the emission above 10 MeV of the brighter afterglows of interest here (see below), thus we will restrict to pair-formation of afterglow photons on other afterglow photons.

For the pair-formation in an un-decelerated source, which is applicable for the external-shock at the peak of its light-curve, we (i.e. I, Panaitescu 2015) have shown that the optical-thickness is

$$\tau(E) = 0.46 \left( \frac{z+1}{3} \right)^6 \frac{\Phi}{10^{-2} \text{cm}^{-2}} \left( \frac{\Gamma}{200} \right)^6 \left( \frac{t}{10 \text{s}} \right)^{-2} \left( \frac{E}{1 \text{GeV}} \right)^\beta \quad (6)$$

where  $\Phi$  is the photon fluence,  $\Gamma$  is the source Lorentz factor, both functions of the observer time  $t$ , and  $\beta$  is the afterglow energy-spectrum slope. The cut-off energy  $E_\tau$  defined by  $\tau(E_\tau) = 1$  is therefore

$$E_\tau = 1.0 \left( \frac{z+1}{3} \right)^{-6} \left( \frac{\Phi}{10^{-2} \text{cm}^{-2}} \right)^{-1} \left( \frac{\Gamma}{175} \right)^6 \left( \frac{t}{10 \text{s}} \right)^2 \text{GeV} \quad (7)$$

assuming  $\beta = 1$ . Given that, for the expected blast-wave energetics (comparable to the burst output) and ambient medium density, afterglows could be even more relativistic than  $\Gamma = 200$  at  $t = 10 \text{s}$ , the above equation shows that a cut-off energy in the LAT range could be seen only for the brightest afterglows in Table 1. If  $E_\tau$  is measured at some time  $t$ , for an afterglow of fluence  $\Phi(t) \sim tF(t)$ , then the source Lorentz factor can be determined:

$$\Gamma_\tau = 175 \frac{z+1}{3} \left( \frac{\Phi}{10^{-2} \text{cm}^{-2}} \frac{E_\tau}{1 \text{GeV}} \right)^{1/6} \left( \frac{t}{10 \text{s}} \right)^{1/3} \quad (8)$$

For the attenuation of a photon-front with itself, the fraction of escaping photons is  $(1 - e^{-\tau})/\tau$ , where  $\tau$  is the above optical-thickness of the entire front (for a photon passing through it), thus an intrinsic  $F_0(E) \propto E^{-\beta}$  emission spectrum becomes an attenuated one:

$$F(E) \propto \frac{1 - \exp[-\tau(E)]}{\tau(E)} E^{-\beta}, \tau(E) = \left( \frac{E}{E_\tau} \right)^\beta \quad (9)$$

therefore

$$F(E) \propto \begin{cases} E^{-\beta} & E \ll E_\tau [\tau(E) \ll 1] \\ \frac{E^{-\beta}}{\tau(E)} \propto E^{-2\beta} & E_\tau \ll E [\tau(E) \gg 1] \end{cases} \quad (10)$$

Thus, the cut-off due to photon-photon absorption is not the exponential reduction expected for a photon passing through the

entire front, but a break to a steeper power-law (hence  $E_\tau$  is just a "break" energy), owing to those photons produced in the outer one optical-depth, which escape unabsorbed.

Equation (7) shows that the photon-attenuation break-energy  $E_\tau$  increases with the light-curve peak epoch and with decreasing peak fluence. Given that there are fewer photons at higher energies, where a spectral break can be lost in statistical fluctuations, the best chance to measure  $E_\tau$  is for fluence-bright LAT light-curve peaks that occur the earliest.

In our sample, we find only two early afterglow spectra that display a softening break, as shown in Figure 5. Their spectra were fit with both a power-law and the attenuated power-law given in equation (9). An  $F$ -test indicates that the break in the 0-20s spectrum of 090902B is not statistically significant, while that of 090926 is just marginal, at  $1\sigma$  confidence level. That is not surprising, considering that the fluxes measured by LAT in the higher energy channels fall short by only two photons relative to the unabsorbed spectrum (the extension to high energy of the power-law fit to the lower-energy fluxes). For the best-fit break energies,  $E_\tau = 20 \text{GeV}$  for 090902B and  $E_\tau = 7 \text{GeV}$  for 090926, and for their peak fluences and redshifts, equation (8) yields about the same source Lorentz factor  $\Gamma_\tau \simeq 400$  at 10 s. Taking into account the large uncertainties in determining those break energies, only lower limits can be set:  $\Gamma > 330$  for 090902B and  $\Gamma > 350$  for 090926.<sup>3</sup>

The attenuated spectra of Figure 5 indicate that a strong evidence for a power-law softening at higher energies requires that each power-law branch is measured over a decade in photon energy and that the highest energy channel has at least one photon. With a  $\Delta E \simeq E$  energy-binning of the spectrum, the number of photons per energy-channel follows  $N(E) \propto E^{-\beta}$ , for an unabsorbed energy-spectrum  $F_0(E) \propto E^{-\beta}$ . Starting with the minimal  $N(10 \text{GeV}) = 1$  photon in the 10 GeV channel, and going toward lower energies with an attenuated  $F(E) \propto E^{-2\beta}$  spectrum, requires  $N(E_\tau) = 10^{2\beta}$  photons at  $E_\tau = 1 \text{GeV}$ . From here, the unabsorbed spectrum would have  $N(0.1 \text{GeV}) = 10^\beta N(1 \text{GeV}) = 10^{3\beta}$  photons which, for an average LAT effective-area of  $9000 \text{cm}^2$  for on-axis photons, implies a fluence  $\Phi = 10^{3\beta-4} \text{cm}^{-2}$ . Thus, for the average spectral slope  $\beta = 1$ , an afterglow spectrum will show good evidence for the photon-attenuation broken power-law with a break at 1 GeV if its fluence at the light-curve peak is  $\Phi = 0.1 \text{cm}^{-2}$ . Ten afterglows shown in Figures 2 and 3 have spectra harder than  $\beta = 1$  and lower peak fluences, with measurements spanning 2-3 decades in energy, but do not show a spectral softening; instead, some display a harder component at higher energies. For those few afterglows with known redshift, equation (8) with  $E_\tau > 10 - 100 \text{GeV}$  can be used to set a lower limit on their Lorentz factor at the light-curve peak.

#### 4.3. Steepening of the synchrotron spectrum

If the electron acceleration mechanism is first order Fermi and if the magnetic field is perpendicular to the shock, then the electron gyration time  $T_L = 2\pi/\omega_L = 2\pi\gamma m_e c^2/eB$  in the down-stream fluid underestimates the time that the electron spends in a high magnetic field  $B$ , while bouncing off an increasing  $B$  or on regions of uniform  $B$  before returning upstream and, then, being deflected in the upstream region and

<sup>3</sup>Ackermann et al (2011) also concluded that the LAT data offer only a weak evidence for a break in the 3-22s spectrum of 090926, and found  $E_\tau = 0.2 \text{GeV}$  for a broken power-law fit and  $E_\tau = 1.4 \text{GeV}$  for an exponential cut-off; using the burst variability timescale  $\Delta t = 0.15 \text{s}$  instead of the peak epoch  $t \simeq 13 \text{s}$ , they inferred a higher Lorentz factor  $\Gamma_\tau = 720$ .

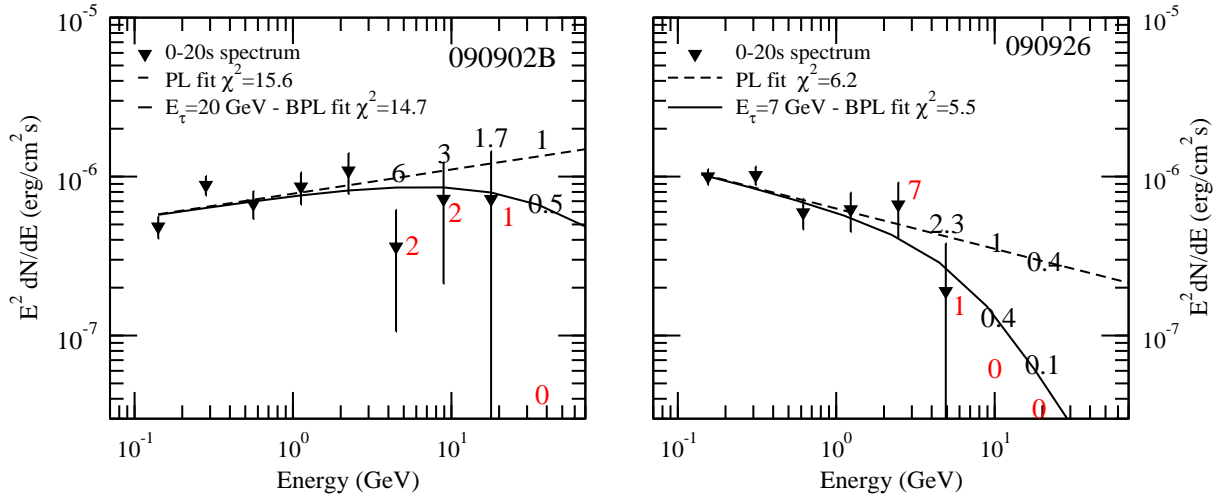


FIG. 5.— Early spectra of the two brightest (in fluence, around light-curve peak) afterglows, showing power-law fits (dashed line) and best-fits including attenuation for pair-formation, with the “cut-off” energies in legends. The cut-off is not exponential, but a transition to a steeper power-law (see text). Black numbers next to lines indicate the model number of photons in that channel; red show the number of LAT photons. The reduction in  $\chi^2$  obtained by the addition of the cut-off corresponds to a chance probability of obtaining that fit improvement of 0.54 for 090902B and 0.35 for 090926. Both break energies are poorly constrained: a  $\Delta\chi^2 = 1$  increase of the best-fit  $\chi^2$  (in legend) sets only lower limits on the break energy:  $E_\tau > 8$  GeV for 090902B and  $E_\tau > 4$  GeV for 090926. Spectra integrated over shorter durations have fewer photons and higher Poisson fluctuations, and do not provide better evidence for a spectral cut-off.

caught by the shock for another energy-gaining shock-crossing. However, if the magnetic field is parallel to the shock, then the Larmor period  $T_L$  is a better approximation for the duration during which the electron loses its energy, because the electron exits the shock after a half-orbit. Thus, the gyration timescale  $T_L$ , which increases with the electron energy  $\gamma m_e c^2$ , brackets the time that an electron spends in the shocked fluid.

Electrons that lose their energy on a synchrotron-cooling timescale (assuming that inverse-Compton losses are weaker,  $Y < 1$ )  $T_{sy} = \gamma m_e c^2 / P_{sy}$ , with the synchrotron power  $P_{sy} = (1/6\pi)\sigma_e c (B\gamma)^2$  for a pitch-angle  $\theta = \pi/2$ , shorter than the time  $\sim T_L(\gamma)$  that they spend in the shocked fluid will not exit the shock and be re-accelerated, thus the condition  $T_{sy}(\gamma) = T_L(\gamma)$  sets an approximate upper-limit on the energy that electrons can acquire through first-order Fermi acceleration:

$$\gamma_s(\pi/2) = \left( \frac{3e}{\sigma_e B} \right)^{1/2} = \frac{24 \text{ TeV}/m_e c^2}{\sqrt{B}} \quad (11)$$

where  $\sigma_e = (8\pi/3)r_e^2$  is the electron scattering cross-section, with  $r_e = e^2/m_e c^2$  being the classical electron radius. Electrons of energy  $\gamma_s(\pi/2)$  radiate synchrotron photons at a characteristic frequency

$$\omega_c[\gamma_s(\pi/2)] = \frac{3e}{2m_e c} [\gamma_s(\pi/2)]^2 B = \frac{27}{16\pi} \frac{c}{r_e} \quad (12)$$

that is independent of the magnetic field strength  $B$ . The corresponding synchrotron-spectrum averaged energy, after a relativistic boost  $\Gamma$  and at a redshift  $z$ , is

$$E_s = 1.7 \frac{3}{z+1} \frac{\Gamma}{100} \text{ GeV} \quad (13)$$

If inverse-Compton is the emission process dominant at LAT energies, then the maximal upscattered photon energy corresponding to the maximal electron energy given in equation (11) is well above the LAT range. However, if the LAT emission process is synchrotron, then the spectral cut-off associated with

the maximal electron energy could fall within the LAT energy range (equation 13), and its measurement determines the source Lorentz factor

$$\Gamma_s \gtrsim 60 \frac{z+1}{3} \frac{E_s}{1 \text{ GeV}} \quad (14)$$

Being softer, the emission of 090926 (Figure 5) is more likely to be synchrotron. If its spectral break arises from the upper-limit on the energy that electrons acquire through shock-acceleration ( $E_s > 4$  GeV), then  $\Gamma > 250$  for 090926 at about 10 s. If also synchrotron emission, the break of 090902B ( $E_s > 8$  GeV) implies  $\Gamma > 440$ .

Given that the synchrotron power depends on the electron pitch-angle,  $P_{sy} \propto \sin^2 \theta$ , the equality of the gyration period with the synchrotron cooling timescale leads to  $\gamma_s(\theta) = \gamma_s(\pi/2)/\sin \theta$ . Thus, electrons that enter the shock with an energy  $\gamma > \gamma_s(\pi/2)$  will lose all their energy in the downstream region if their pitch-angle satisfies  $\theta > \theta_c(\gamma) \equiv \sin^{-1}[\gamma_s(\pi/2)/\gamma]$  and will not cross the shock again and will not be re-accelerated. Conversely, electrons with pitch-angles satisfying  $\theta < \theta_c(\gamma)$  will not lose all their energy before going back to the upstream region, thus such electrons could be accelerated to energies higher than their current  $\gamma$ . If the pitch-angle distribution is isotropic, then a fraction  $f(\gamma) = 1 - \cos \theta_c(\gamma) = 1 - \sqrt{1 - [\gamma_s(\pi/2)/\gamma]^2}$  of the current generation of electrons with  $\gamma > \gamma_s(\pi/2)$  will go to the next shock-crossing. Together with that the escape of electrons in the downstream region and in the loss-cone in the upstream lead to a power-law distribution with energy ( $dN_e/d\gamma \propto \gamma^{-p}$ ), the radiative cooling for electrons with  $\gamma > \gamma_s(\pi/2)$  means that, at  $\gamma_s(\pi/2)$ , the electron distribution steepens from  $dN_e/d\gamma \propto \gamma^{-p}$  to  $dN_e/d\gamma \propto \gamma^{-p}\{1 - \sqrt{1 - [\gamma_s(\pi/2)/\gamma]^2}\}$ , which is  $dN_e/d\gamma \propto \gamma^{-(p+2)}$  for  $\gamma \gg \gamma_s(\pi/2)$ . Because the slope of the synchrotron spectrum is  $\beta = (p-1)/2$ , a steepening of the electron distribution by  $\Delta p = 2$  corresponds to a spectral softening by  $\Delta\beta = 1$ . Thus, the synchrotron spectrum including the effect of electron radiative cooling during its acceleration (i.e. during one gyra-

tion timescale) is

$$F(E) \propto \begin{cases} E^{-\beta} & E \ll E_s \\ E^{-(\beta+1)} & E_s \ll E \end{cases} \quad (15)$$

with  $E_s$  given in equation (13). For the average spectral slope  $\beta = 1$ , the steepening of the synchrotron spectrum at  $E_s$  due to electron cooling during one gyration period<sup>4</sup> given in equation (15) is the same as the softening at  $E_\tau$  due to photon-photon absorption given in equation (10).

Thus, LAT measurements of afterglow spectral breaks are unlikely to distinguish between the above two processes/mechanisms.

## 5. CONCLUSIONS

We have presented the light-curves and spectra of 24 Fermi-LAT afterglows observed in the first  $7^{2/3}$  years of operation (Figures 2 and 3). The only selection criterion was that the light-curve was monitored over at least a decade in time. The reason for that is to allow the determination of the flux power-law decay and compare it with the spectral power-law slope. The average index of flux power-law decay for this set is  $\bar{\alpha} = 1.2 \pm 0.4$ . Together with that the celestial background is approximately  $10^{-5.5}$  photons/s above 100 MeV, in a  $5^\circ$  region around the afterglow (the LAT PSF at 100 MeV), the above selection criterion implies that only afterglows brighter than about  $10^{-4}$  photons/s at peak or at first observation were retained. The price to pay for that severe selection is the exclusion of 80 percent of afterglows seen by LAT, which were too dim or decayed too fast.

Consequently, our selection criterion excludes dimmer afterglows with a fast decay and induces a brightness–decay correlation. Still, as shown in Figure 4, six out of the seven brightest afterglows are fast-decayers, displaying a power-law decay index  $\alpha > 1.2$  (the exception being 130427), thus the brightness–decay correlation is real. A similar correlation has been observed for optical afterglows (Panaitescu & Vestrand 2008) and has been attributed to how energy is deposited in the external-shock: short-lived ejecta outflows arrive quickly at the forward-shock and power bright afterglows, long-lived outflows deposit their energy slower and produce afterglows that are dimmer initially and which decay slower.

Therefore, the bright/fast-decaying–dim/slow-decaying dichotomy of LAT afterglows could be one piece of evidence for a long-lived energy-injection in some afterglows, a process which was found to occur in a large fraction of Swift X-ray afterglows (Panaitescu & Vestrand 2012). About one third of the LAT afterglows in our sample show a light-curve decay slower than expected for the synchrotron forward-shock emission and an impulsive ejecta release (Figure 4), although often consistent with it, due to the large uncertainties of the flux decay indices and/or spectral slopes. That is a second evidence for the energy-injection in afterglows that an extended ejecta-release would yield.

The average slope of LAT afterglow spectra at lower energies (0.1–1 GeV) is  $\bar{\beta} = 1.0 \pm 0.3$ , with five afterglows (130327B, 131231, 150523, 150627, 160509) clearly being harder than  $\beta = 1$  (i.e. their output peaks at a photon energy above LAT’s range). Given that the inverse-Compton spectrum below the upscattered synchrotron cooling break is harder by  $\Delta\beta = 0.5$  than the synchrotron emission above the cooling break, we propose that the LAT emission of the hardest afterglows is inverse-Compton. A better evidence for the latter spectral component is provided by six afterglows (Table 2: 090328, 100414, 110721, 110731, 130427, 140619B) whose spectrum hardens above a dip energy of 0.3 – 3 GeV, indicating that synchrotron is dominant below the dip and inverse-Compton above it. In all, we find evidence for inverse-Compton emission being detected in 11 out of the 24 LAT afterglows considered here.

The early spectrum of one afterglow displays a softening, which could be due to either photon-photon absorption in the source or to a maximal energy that electrons acquire in afterglow shocks.<sup>5</sup> The former process softens the power-law  $F(E) \propto E^{-\beta}$  afterglow spectrum by  $\Delta\beta = \beta$  at the break-energy given in equation (7), the latter by a comparable  $\Delta\beta = 1$  at the break-energy given in equation (13). For each mechanism, a measurement of the break-energy determines the afterglow Lorentz factor (equations 8 and 14), while single power-law spectra setting only a lower-limit on  $\Gamma$ .

This work made use of the LAT data and Science Tools available at the Fermi Science Support Center, <http://fermi.gsfc.nasa.gov/ssc/data/>

## REFERENCES

- Abdo A. et al, 2009a, *Sci* 323, 1688  
 Abdo A. et al, 2009b, *ApJ* 706, L138  
 Ackermann M. et al, 2010a, *ApJ* 716, 1178  
 Ackermann M. et al, 2010b, *ApJ* 717, L127  
 Ackermann M. et al, 2011, *ApJ* 729, 114  
 Ackermann M. et al, 2013a, *ApJS* 209, 11  
 Ackermann M. et al, 2013b, *ApJ* 763, 71  
 Ackermann M. et al, 2014, *Sci* 343, 42  
 Atwood, W. et al, 2009, *ApJ* 697, 1071  
 Axelsson M. et al, 2012, *ApJ* 757, L31  
 Fan Y-Z et al, 2013, *ApJ* 776, 95  
 Ghirlanda G., Ghisellini G., Nava L., 2010, *A&A* 510, L7  
 Giuliani A. et al, 2010, *ApJ* 708, L84  
 Giuliani A. et al, 2014, *A&AL*, submitted ([lanl.arxiv.org/abs/1407.0238](http://lanl.arxiv.org/abs/1407.0238))  
 Kumar P., Barniol Duran R., 2009, *MNRAS* 409, 226  
 Kumar P., Zhang B., 2015, *PhR* 561, 1  
 Liang, Y-F et al, 2014, *ApJ* 781, L74 (2014)  
 Liu B. et al, 2014, *ApJ* 787, L6  
 Mészáros P., Rees M., 1997, *ApJ* 476, 232  
 Nousek J. et al, 2006, *ApJ*, 642, 389  
 Panaitescu A., 2007, *MNRAS* 379, 331  
 Panaitescu A., Vestrand T., 2008, *MNRAS* 387, 497  
 Panaitescu A., Vestrand T., 2011, *MNRAS* 414, 3537  
 Panaitescu A., Vestrand T., 2012, *MNRAS* 425, 1669  
 Panaitescu A., Vestrand T., Wozniak P., 2013, *MNRAS* 433, 759  
 Panaitescu A., 2015, *ApJ* 806, 64  
 Rees M., Mészáros P., 1998, *ApJ* 496, L1  
 Swenson C. et al., 2010, *ApJ* 718, L14  
 Tam P.-H. et al, 2013, *ApJ* 772, L4

<sup>4</sup>Not to be confused with the softening of the synchrotron spectrum by  $\Delta\beta = 1/2$  due to electron cooling during one dynamical timescale, which is at a much lower energy than  $E_s$ .

<sup>5</sup>Other mechanisms for a spectral softening – the onset of Klein-Nishina regime for inverse-Compton scatterings and attenuation by the EBL – should both yield breaks above the LAT range

TABLE 3

Light-curves of Figures 2 and 3. Flux  $1\sigma$  upper limits (not tabulated) correspond to 1.9 photons for each time-bin

GRB	time (s)	Flux ( $\text{cm}^{-2} \text{s}^{-1}$ )	$\pm\Delta t$ (s)	$\sigma(F)$ ( $\text{cm}^{-2} \text{s}^{-1}$ )	time (s)	Flux ( $\text{cm}^{-2} \text{s}^{-1}$ )	$\pm\Delta t$ (s)	$\sigma(F)$ ( $\text{cm}^{-2} \text{s}^{-1}$ )	time (s)	Flux ( $\text{cm}^{-2} \text{s}^{-1}$ )	$\pm\Delta t$ (s)	$\sigma(F)$ ( $\text{cm}^{-2} \text{s}^{-1}$ )
080916C	3	1.4e-4	1	3.2e-4	6	4.3e-3	2	5.4e-4	12	1.4e-3	4	2.2e-4
	24	1.0e-3	8	1.3e-4	48	3.4e-4	16	5.4e-5	96	1.5e-4	32	2.6e-5
	192	5.2e-5	64	1.1e-5	384	1.6e-5	128	4.1e-6	768	7.2e-6	256	1.9e-6
	1536	3.5e-6	512	1.0e-6	3072	4.4e-6	1024	2.4e-6	12288	3.1e-6	4096	5.9e-7
090217	6	2.6e-4	2	1.7e-4	12	1.5e-4	4	9.2e-5	24	7.8e-5	8	4.7e-5
	48	2.0e-5	16	1.9e-5	96	1.0e-5	32	1.0e-5	192	5.8e-6	64	5.7e-6
	384	5.4e-6	128	4.3e-6	768	2.9e-6	256	6.7e-6	6144	1.7e-6	2048	1.6e-6
090328	12	1.5e-4	4	2.0e-4	24	1.1e-4	8	1.1e-4	48	3.3e-5	16	4.4e-5
	96	4.9e-5	32	2.4e-5	192	2.0e-5	64	5.8e-6	384	1.9e-5	128	3.7e-6
	768	8.4e-6	256	1.8e-6	1536	4.3e-6	512	8.8e-7	3072	3.5e-6	1024	1.0e-6
090510	0.75	3.2e-4	0.25	7.3e-4	1.5	1.4e-2	0.5	1.5e-3	3	7.3e-3	1	7.6e-4
	6	9.8e-4	2	2.0e-4	12	3.1e-4	4	7.8e-5	24	9.8e-5	8	4.2e-5
	48	5.3e-5	16	1.6e-5	96	1.4e-5	32	8.5e-6	192	1.1e-5	64	4.8e-6
	384	3.5e-6	128	2.1e-6	768	2.3e-6	256	1.2e-6	1536	2.7e-6	512	6.5e-7
090902B	0.75	5.1e-4	0.25	1.2e-3	3	1.0e-3	1	5.0e-4	6	1.9e-3	2	3.5e-4
	12	4.7e-3	4	3.9e-4	24	1.5e-3	8	1.6e-4	48	4.2e-4	16	5.5e-5
	96	1.4e-4	32	2.0e-5	192	5.1e-5	64	7.8e-6	384	2.5e-5	128	3.9e-6
	768	1.1e-5	256	1.8e-6	3072	5.3e-6	1024	1.2e-6	6144	3.9e-6	2048	4.4e-7
090926	3	2.5e-4	1	3.3e-4	6	3.3e-3	2	4.5e-4	12	5.3e-3	4	4.0e-4
	24	1.1e-3	8	1.3e-4	48	3.3e-4	16	5.1e-5	96	1.1e-4	32	2.1e-5
	192	4.8e-5	64	1.1e-5	3072	4.8e-6	1024	9.0e-7	6144	4.6e-6	2048	7.2e-7
091003	1.5	1.8e-4	0.5	4.1e-4	6	1.3e-4	2	1.3e-4	12	4.4e-5	4	5.9e-5
	24	2.2e-5	8	2.9e-5	48	2.2e-5	16	1.8e-5	96	1.4e-5	32	9.5e-6
	192	7.1e-6	64	4.8e-6	384	8.3e-6	128	2.4e-6	768	2.7e-6	256	1.3e-6
	1536	2.5e-6	512	1.33e-6	6144	1.6e-6	2048	3.0e-7	12288	1.8e-6	4096	2.8e-7
100414	15	7.6e-5	5	1.8e-4	30	2.9e-4	10	1.4e-4	60	1.5e-4	20	4.3e-5
	120	2.9e-5	40	1.3e-5	240	1.7e-5	80	4.2e-6	480	5.7e-6	160	1.6e-6
	960	1.9e-6	320	9.2e-7	1920	3.0e-6	640	6.3e-7	3840	3.3e-6	1280	6.8e-7
110721	0.75	3.1e-3	0.25	1.6e-3	1.5	2.0e-3	0.5	8.4e-4	3	4.9e-4	1	3.3e-4
	6	2.4e-4	2	1.6e-4	12	9.7e-5	4	7.7e-5	24	4.8e-5	8	3.8e-5
	48	1.7e-5	16	1.7e-5	96	1.0e-5	32	8.0e-6	192	7.1e-6	64	4.2e-6
	384	5.4e-6	128	2.5e-6	768	2.7e-6	256	1.3e-6	3072	2.1e-6	1024	4.1e-7
110731	4	8.5e-4	1	3.6e-4	7.5	1.2e-3	2.5	2.0e-4	15	1.4e-4	5	6.8e-5
	30	5.1e-5	10	3.1e-5	60	2.1e-5	20	1.4e-5	120	6.4e-6	40	6.2e-6
	240	3.2e-6	80	3.2e-6	480	4.3e-6	160	2.1e-6	960	3.3e-6	320	9.4e-7
130327B	7.5	5.2e-5	2.5	1.2e-4	30	1.9e-4	10	4.9e-5	60	7.9e-5	20	2.2e-5
	120	3.5e-5	40	9.6e-6	240	5.5e-6	80	3.8e-6	480	4.9e-6	160	2.2e-6
	1920	3.6e-6	640	8.3e-6	3840	5.5e-6	1280	2.3e-6	7680	1.4e-6	2560	5.9e-7
130427	5.5	5.8e-4	4.5	1.4e-4	15	1.8e-3	5	2.4e-4	30	1.2e-3	10	1.4e-4
	60	4.8e-4	20	6.0e-5	120	2.9e-4	40	3.0e-5	240	1.7e-4	80	1.5e-5
	480	8.7e-5	160	8.2e-6	3840	5.9e-6	1280	7.9e-7	7680	3.2e-6	2560	5.4e-7
130821	48	3.2e-5	16	2.2e-5	96	2.5e-5	32	1.2e-5	192	1.7e-5	64	4.9e-6
	384	1.6e-5	128	3.2e-6	768	5.2e-6	256	1.3e-6	1536	3.6e-6	512	8.0e-7
	3072	2.8e-6	1024	2.2e-6	6144	2.2e-6	2048	3.6e-7	12288	1.1e-6	4096	2.9e-7
131108	1.5	2.8e-3	0.5	6.7e-4	3.5	1.2e-3	1.5	2.5e-4	7.5	2.1e-3	2.5	2.6e-4
	15	4.8e-4	5	8.8e-5	30	1.5e-4	10	3.4e-5	60	3.6e-5	20	1.6e-5
	120	7.8e-6	40	6.2e-6	240	4.6e-6	80	3.1e-6	480	5.6e-6	160	1.6e-6
131231	24	3.0e-5	8	4.1e-5	48	5.3e-5	16	2.9e-5	96	2.5e-5	32	1.4e-5
	192	1.9e-5	64	5.3e-6	384	4.5e-6	128	2.7e-6	768	3.5e-6	256	1.6e-6
140206	12	2.3e-4	4	1.2e-4	24	1.5e-4	8	6.7e-5	48	1.6e-5	16	2.2e-5
	96	2.6e-5	32	1.4e-5	192	4.6e-6	64	4.5e-6	384	8.8e-6	128	2.4e-6
	768	4.8e-6	256	1.3e-6	1536	3.8e-6	512	8.3e-7	3072	4.6e-6	1024	9.8e-7
140523	1.5	3.4e-4	0.5	7.9e-4	3	3.4e-4	1	4.5e-4	6	8.7e-5	2	2.0e-4
	12	2.7e-4	4	1.6e-4	24	2.4e-4	8	7.3e-5	48	9.1e-5	16	4.5e-5
	96	2.4e-5	32	1.9e-5	192	3.3e-5	64	1.5e-5	384	3.0e-5	128	1.3e-5
140619B	0.17	2.8e-3	0.075	3.7e-3	0.37	5.8e-3	0.12	3.1e-3	0.75	2.5e-3	0.25	1.5e-3
	1.5	1.0e-3	0.5	7.1e-4	3	2.1e-4	1	2.8e-4	12	2.6e-5	4	6.0e-5
	24	1.3e-5	8	3.0e-5	192	1.5e-6	64	3.6e-6	384	7.6e-7	128	1.8e-6
141028	0.75	4.0e-4	0.25	9.3e-4	3	3.0e-4	1	2.9e-4	6	1.5e-4	2	1.5e-4
	12	1.0e-4	4	7.9e-5	24	2.5e-5	8	3.3e-5	48	2.4e-5	16	1.9e-5
	96	1.2e-5	32	9.3e-6	192	1.3e-5	64	7.2e-6	384	8.2e-6	128	5.6e-6
150523	3	9.5e-5	1	2.2e-4	6	9.5e-5	2	1.3e-4	12	1.9e-4	4	9.4e-5
	24	7.1e-5	8	4.3e-5	48	5.4e-5	16	2.5e-5	96	2.4e-5	32	1.2e-5
	192	1.4e-5	64	4.3e-6	384	5.7e-6	128	2.6e-6	768	3.6e-6	256	1.1e-6
150627	24	1.2e-4	8	2.9e-4	48	5.2e-5	16	1.2e-4	96	3.9e-5	32	3.8e-5
	192	2.9e-5	64	7.4e-6	384	8.0e-6	128	2.3e-6	768	5.3e-6	256	1.3e-6
	1536	4.4e-6	512	8.9e-7	3072	2.4e-6	1024	5.0e-7	6144	3.2e-6	2048	4.2e-7
150902	6	4.5e-4	2	2.2e-4	12	2.5e-4	4	1.2e-4	24	1.1e-4	8	5.5e-5
	48	2.8e-5	16	2.2e-5	96	2.9e-5	32	1.3e-5	192	1.3e-5	64	6.1e-6
	384	1.2e-5	128	2.9e-6	768	4.4e-6	256	1.3e-6	1536	3.7e-6	512	7.8e-7
160325	6	4.4e-5	2	1.0e-4	48	1.1e-5	16	1.5e-5	96	2.9e-5	32	1.2e-5
	192	8.6e-6	64	5.1e-6	384	4.6e-6	128	2.7e-6	768	3.2e-6	256	1.6e-6
160509	12	5.9e-4	4	1.3e-4	24	8.7e-4	8	1.1e-4	48	2.6e-5	16	2.1e-5
	96	2.2e-5	32	1.2e-5	192	1.6e-5	64	4.9e-6	384	5.3e-6	128	2.8e-6
	768	6.0e-6	256	1.5e-6	1536	2.5e-6	512	6.5e-7	3072	1.5e-6	1024	1.5e-6

TABLE 4

Spectra of Figures 2 and 3 ( $1\sigma$  upper limits, corresponding to 1.9 photons, are not tabulated). Fluxes are in  $erg/cm^2s$ ;  $1\sigma$  upper uncertainty  $\sigma_+$  is given in parenthesis. For fluxes above several photons per energy channel per time-bin, upper and lower uncertainties are about equal ( $\sigma_+ \simeq \sigma_-$ ) but, for fluxes of a few photons,  $\sigma_- < \sigma_+$ .

GRB	time (s)	F(0.14k) ( $\sigma_+$ )	F(0.28k) ( $\sigma_+$ )	F(0.56k) ( $\sigma_+$ )	F(1.1k) ( $\sigma_+$ )	F(2.2k) ( $\sigma_+$ )	F(4.5k) ( $\sigma_+$ )	F(8.9k) ( $\sigma_+$ )	F(18k) ( $\sigma_+$ )	F(35k) ( $\sigma_+$ )	F(71k) ( $\sigma_+$ )
080916C	10-100	1.2e-7 (1.8e-8)	1.0e-7 (1.9e-8)	1.4e-7 (2.9e-8)	1.2e-7 (3.3e-8)	7.7e-8 (6.1e-8)	3.8e-8 (8.9e-8)	1.5e-7 (2.0e-7)		3.1e-7 (7.1e-7)	
090217	0-100	1.2e-8 (4.6e-9)	1.5e-8 (6.1e-9)	1.2e-8 (1.1e-8)	6.6e-9 (1.5e-8)						
090328	10-1000	4.7e-9 (9.0e-10)	4.2e-9 (1.0e-9)	3.1e-9 (1.1e-9)	2.0e-9 (2.0e-9)	5.2e-9 (4.1e-9)	1.3e-8 (8.9e-9)	5.2e-9 (1.2e-8)			
090510	0-10	6.3e-7 (9.4e-8)	8.8e-7 (1.3e-7)	7.6e-7 (1.6e-7)	8.6e-7 (2.1e-7)	1.3e-6 (3.7e-7)	6.4e-7 (6.3e-7)	4.2e-7 (9.8e-7)		1.7e-6 (3.9e-6)	
090902B	10-100	9.3e-8 (1.5e-8)	2.1e-7 (2.6e-8)	1.8e-7 (3.1e-8)	1.9e-7 (4.1e-8)	3.5e-7 (7.7e-8)	2.4e-7 (1.3e-7)	1.4e-7 (1.8e-7)	5.5e-7 (4.4e-7)	2.7e-7 (6.4e-7)	
090902B	100-1000	7.4e-9 (1.2e-9)	6.5e-9 (1.3e-9)	5.1e-9 (1.5e-9)	5.7e-9 (2.8e-9)	5.7e-9 (4.5e-9)	1.4e-8 (9.6e-9)		1.1e-8 (2.6e-8)		
090926	10-100	1.9e-7 (2.3e-8)	2.6e-7 (3.2e-8)	1.9e-7 (3.4e-8)	1.9e-7 (4.4e-8)	2.5e-7 (7.1e-8)	1.6e-7 (1.3e-7)	8.2e-8 (1.9e-7)	1.6e-7 (3.8e-7)		
090103	0-100	8.5e-9 (3.5e-9)	6.1e-9 (6.0e-9)	6.3e-9 (8.4e-9)	5.3e-9 (1.2e-8)	2.1e-8 (2.8e-8)					
100414	10-1000	2.2e-9 (5.9e-10)	2.6e-9 (7.5e-10)	1.7e-9 (1.1e-9)	2.9e-9 (1.9e-9)	1.1e-9 (2.6e-9)	4.5e-9 (6.0e-9)			3.6e-8 (4.8e-8)	
110721	0-10	2.5e-7 (6.7e-8)	7.7e-8 (7.5e-8)	4.0e-8 (9.3e-8)	1.3e-7 (1.8e-7)			5.3e-7 (1.2e-6)			
110731	0-100	4.7e-8 (8.0e-9)	2.9e-8 (7.5e-9)	1.8e-8 (7.4e-9)	3.6e-8 (1.4e-8)	4.1e-8 (3.2e-8)					
130327B	0-150	9.5e-9 (3.4e-9)	1.5e-8 (5.1e-9)	1.3e-8 (9.0e-9)	2.2e-8 (1.5e-8)	3.6e-8 (2.8e-8)	3.6e-8 (4.8e-8)	3.6e-8 (8.3e-8)			
130427	1-20	3.5e-7 (6.8e-8)	2.5e-7 (6.9e-8)	2.7e-7 (1.2e-7)	1.5e-7 (1.5e-7)	2.0e-7 (2.6e-7)		7.9e-7 (1.0e-6)			3.2e-6 (7.3e-6)
130427	20-100	1.1e-7 (1.9e-8)	1.5e-7 (2.6e-8)	1.6e-7 (3.4e-8)	2.2e-7 (5.1e-8)	2.2e-7 (1.0e-7)	2.4e-7 (1.6e-7)	4.8e-7 (3.3e-7)	1.9e-7 (4.4e-7)	1.2e-6 (1.1e-6)	
130427	100-600	4.3e-8 (4.4e-9)	4.3e-8 (5.2e-9)	3.7e-8 (6.1e-9)	3.7e-8 (7.9e-9)	1.7e-8 (1.1e-8)	4.0e-8 (2.4e-8)	4.0e-8 (3.9e-8)	5.4e-8 (7.1e-8)	5.3e-8 (1.2e-7)	2.1e-7 (2.8e-7)
130821	30-1000	5.0e-9 (1.1e-9)	4.8e-9 (1.3e-9)	5.3e-9 (1.7e-9)	1.8e-9 (1.7e-9)	1.8e-9 (2.4e-9)	3.5e-9 (4.1e-9)				
131108	10-100	3.9e-8 (7.9e-9)	2.8e-8 (8.0e-9)	1.1e-8 (1.1e-8)	1.2e-8 (1.6e-8)						
131231	10-1000	5.3e-9 (1.8e-9)	5.9e-9 (2.2e-9)	7.9e-9 (3.2e-9)	4.5e-9 (5.9e-9)	8.9e-9 (1.2e-8)	1.8e-8 (2.4e-8)	1.8e-8 (4.1e-8)		7.0e-8 (1.6e-7)	
140206	10-500	4.2e-9 (1.2e-9)	3.0e-9 (1.2e-9)	3.9e-9 (2.6e-9)		2.6e-9 (6.0e-9)	5.2e-9 (1.2e-8)				
140523	10-500	2.2e-9 (2.9e-9)	1.5e-8 (4.9e-9)	1.2e-8 (8.2e-9)	1.2e-8 (1.2e-8)	2.4e-8 (2.4e-8)		3.2e-8 (7.5e-8)			
140619B	0-20	5.9e-8 (2.4e-8)	5.6e-8 (4.5e-8)	6.6e-8 (6.4e-8)	3.7e-8 (8.6e-8)				5.9e-7 (1.4e-6)		
141028	0-500	3.2e-9 (1.1e-9)	4.1e-9 (1.5e-9)	3.6e-9 (2.9e-9)	3.1e-9 (4.1e-9)		6.1e-9 (1.4e-8)				
150523	0-1000	2.3e-9 (5.8e-10)	2.4e-9 (7.1e-10)	3.4e-9 (1.1e-9)	2.8e-9 (1.9e-9)	4.5e-9 (3.6e-9)	4.5e-9 (6.0e-9)	4.5e-9 (1.0e-8)			
150627	10-1000	8.8e-10 (6.0e-10)	1.8e-9 (6.6e-10)	1.2e-9 (1.1e-9)	2.6e-9 (2.1e-9)	6.6e-9 (4.5e-9)	1.3e-8 (8.9e-9)	5.2e-9 (1.2e-8)			
150902	5-500	6.6e-9 (1.5e-9)	6.9e-9 (1.9e-9)	3.8e-9 (2.6e-9)	2.6e-9 (3.4e-9)	5.2e-9 (6.9e-9)	5.2e-9 (1.2e-8)	1.0e-8 (2.4e-8)			
160325	100-1000	1.2e-9 (5.2e-10)	8.7e-10 (5.9e-10)	1.4e-9 (9.2e-10)	4.6e-10 (1.1e-9)	1.8e-9 (2.4e-9)					
160509	33-1000	2.1e-9 (5.7e-10)	3.6e-9 (9.1e-10)	2.1e-9 (1.3e-9)	5.4e-9 (2.5e-9)	4.7e-9 (3.8e-9)	4.7e-9 (6.3e-9)	4.7e-9 (1.1e-8)		1.9e-8 (4.4e-8)	3.8e-8 (8.7e-8)